星形成ゼミ20210205

SFN #335 15-21

片岡章雅

15. A new prolonged decrease event in the brightness of the young stellar object V2492 Cygni, Sunay Ibryamov et al.

16. The Cloud Factory II: Gravoturbulent Kinematics of Resolved Molecular Clouds in a Galactic Potential, Andres F. Izquierdo et al.

17. Evolution of the density PDF in star forming clouds: the role of gravity, Etienne Jaupart et al.

18. Star Formation Efficiency and Dispersal of Giant Molecular Clouds with UV Radiation Feedback: Dependence on Gravitational Boundedness and Magnetic Fields, Jeong-Gyu Kim, et al.

19. The CARMA-NRO Orion Survey: Filament Formation via Collision-Induced Magnetic Reconnection – The Stick in Orion A, Shuo Kong, et al.

20. Probing the Cold Deep Depths of the California Molecular Cloud: The Icy Relationship between CO and Dust, John Arban Lewis et al.

21. Characterization of very wide companion candidates to young stars with planets and disks, F. Z. Majidi, et al.

20. Probing the Cold Deep Depths of the California Molecular Cloud: The Icy Relationship between CO and Dust, John Arban Lewis et al.

We study the relationship between molecular gas and dust in the California Molecular Cloud over an unprece- dented dynamic range of cloud depth (AV = 3 – 60 magnitudes). We compare deep Herschel-based measure- ments of dust extinction with observations of the 12CO, 13CO, and C18O J=2-1 lines on sub-parsec scales across the cloud. We directly measure the ratio of CO integrated intensity to dust extinction to derive the CO X-factor at over 105 independent locations in the cloud. Confirming an earlier study, we find that no single 12CO X-factor can characterize the molecular gas in the cold (Tdust ≤ 20) regions of the cloud that account for most of its mass. We are able to derive a single-valued X-factor for all three CO isotopologues in the warm (Tdust >25 K) material that is spatially coincident with an H II region surrounding the star LkHα 101. We derive the LTE CO column densities for 13CO and C18O since we find both lines are relatively optically thin. In the warm cloud material CO is completely in the gas phase and we are able to recover the total 13CO and C18O abundances. Using CO abundances and deep Herschel observations, we measure lower bounds to the freeze-out of CO onto dust across the whole cloud finding some regions having CO depleted by a factor of > 20. We construct the first maps of depletion that span the extent of a giant molecular cloud. cores and discuss their physical nature.

アブストラクト

Av=3-60の大きなダイナミックレンジで、California Molecular Cloudを観測した。

観測データ：ハーシェルのダスト減光と、12CO, 13CO, C18O

目的：10^5箇所の独立な場所でCO X-factorを導出した。

結果：

Tdust < 20Kの冷たい領域では、CO X-factorは単純な1パラメータではない。

Tdust < 25K の暖かい場所では、single valueのCO X-factorを導出した

LTEを仮定して、13COとC18Oの密度を出した。光学的に薄い。温かい領域では、COは全部気相にあると仮定して良さそう。

COの凝結についても調べた。場所によっては>20くらいdepletionしてる。

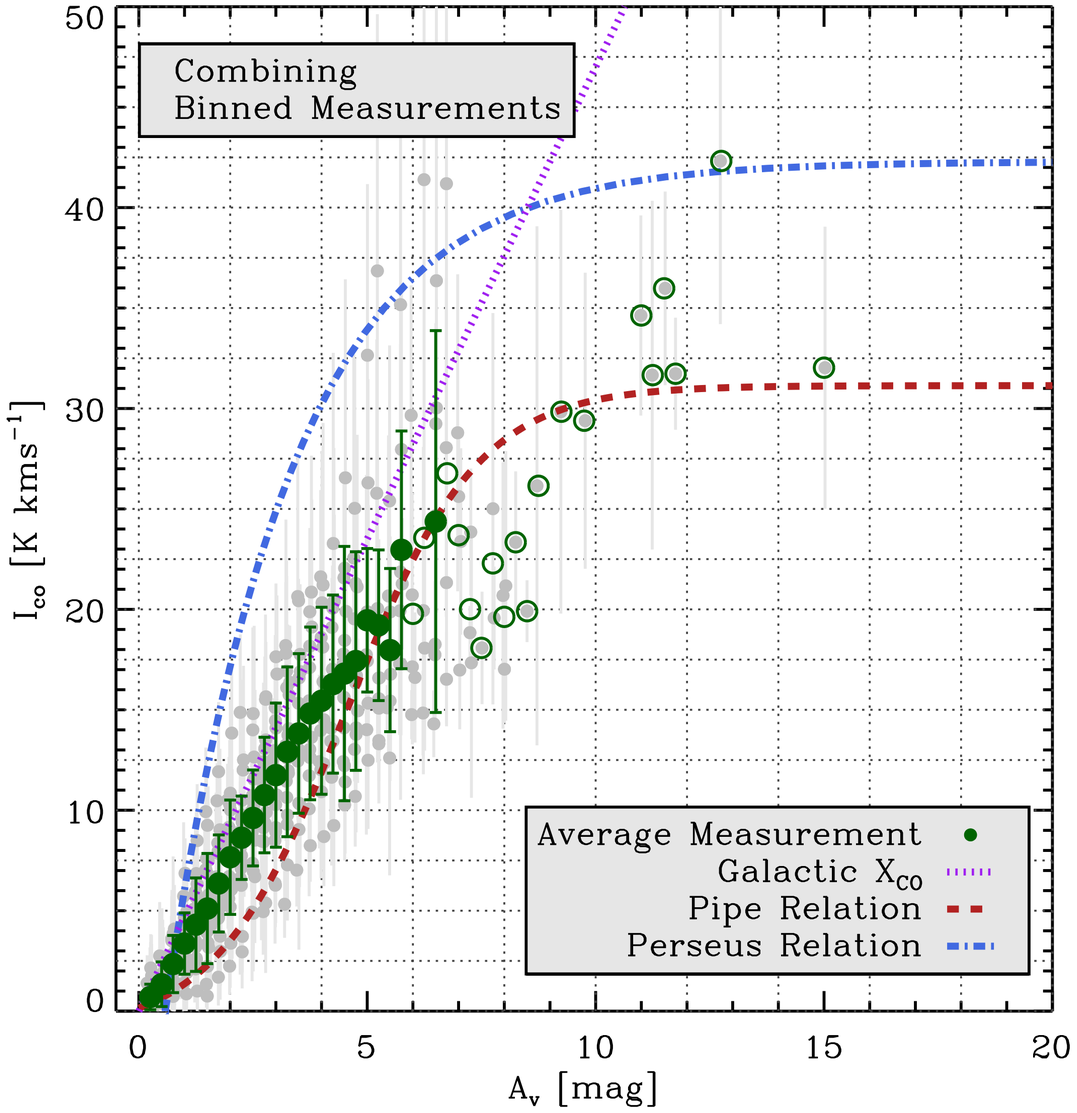

Lee et al. 2014

イントロ
通常X-factorは12COを用いて、GMCの比較的面密度の低いところ(Av<4-5)で求められている。

先行研究：Kong et al.. Av~35までについてX-factorを出した。Tex>18Kのところではsingle X-factorを導出した。ただし、これらはHII regionのある場所と一致している。

この研究は Kong et al. 2015の拡張。まず、ハーシェル使ってAv=3-60のダイナミックレンジで観測。COで観測した領域は3倍大きい。星形成が活発じゃない領域も含まれる。温度はハーシェルを使った。

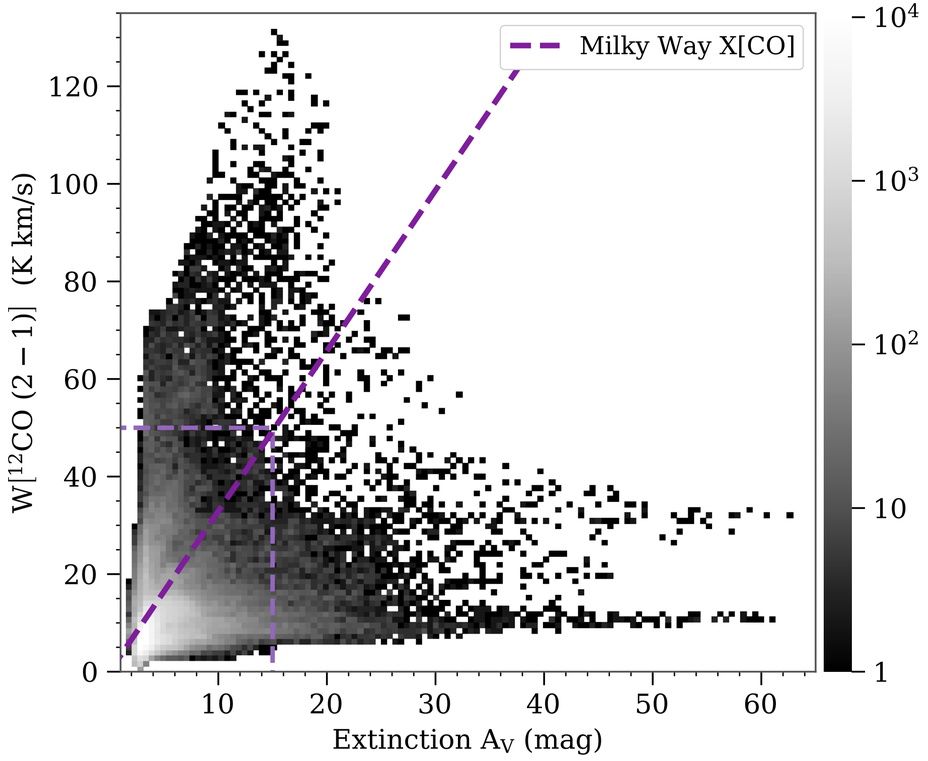

Figure 3. Binned 2D histogram for W[^{12}CO (2−1)] vs A_V for the entire California cloud where W[^{12}CO] is detected at greater than 3σ ($\gtrsim$ 1K). The gray dashed line is the standard relation for the adopted MW X-factor (2×10^{20}cm^{-2} (K km/s)$^{-1}$) which is 3.29 K km/s mag^{-1}. The blue histogram shows the number of pixels in a binned pixel of the plot on a log scale. The black dashed box shows the region containing the bulk of data range covered by previous studies (e.g., Pineda et al. 2008; Ripple et al. 2013).

観測

Arizona Radio Observatory (ARO) 10 m Heinrich-Hertz Sub-millimeter Telescope (SMT), とハーシェル PACS 160 μm and SPIRE 250, 350, and 500 μm をつかったが、分解能は500μm似合わせて36秒角。

H2の出し方

modified BB でフィット。τ850を出して、それを適当にA_Kになおして(Lombardi 2009)、それをN[H2]/Av の値を古典的なものを仮定して(Bohlin 1978, Rachford 2002)出した。最終マップは38”分解能、0.08pcに対応（天体までの距離は450pc）

結果、ハーシェルから導出した質量は5.52×10^4 M⊙ で、クラウド全体の20%くらい。

CO観測について

The average RMS noise per 0.3 km/s channel we achieve is 0.11 K for C18O, 0.13 K for 13CO, and 0.11 K for 12CO.

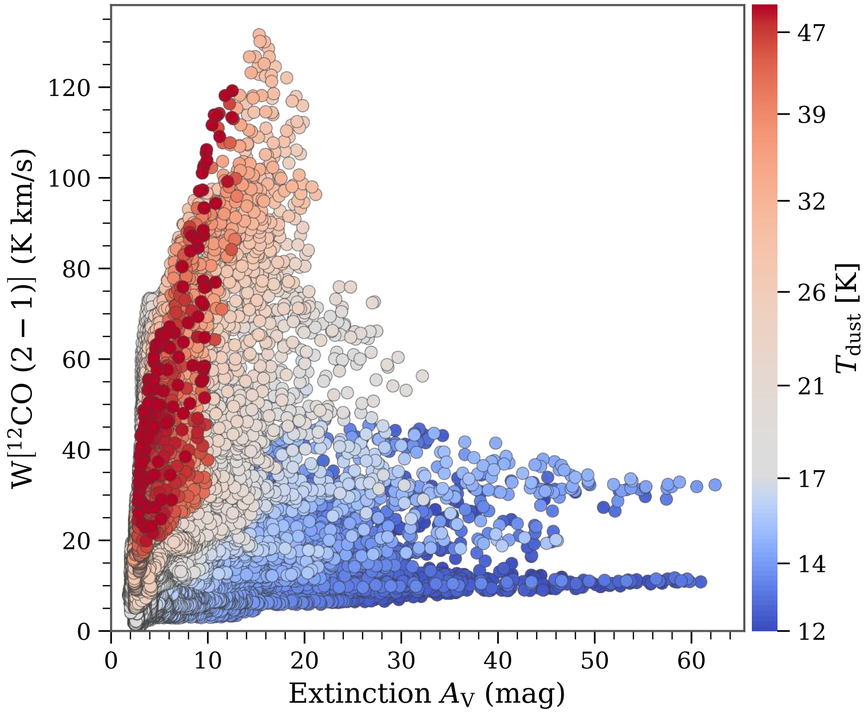

Figure 4. W[^{12}CO(2−1)] vs A_V for the entire California cloud where W[^{12}CO] is detected at greater than 3σ ($\gtrsim$ 1 K). The points are colored by their *Herschel*-derived dust temperature (T_{dust}). The points are plotted so that hotter points are plotted over cooler points.

ハーシェルの温度で色分けしてみると、温かいところは線形な関係がありそう。
25K以上のところはH II region in L1482 と一致。

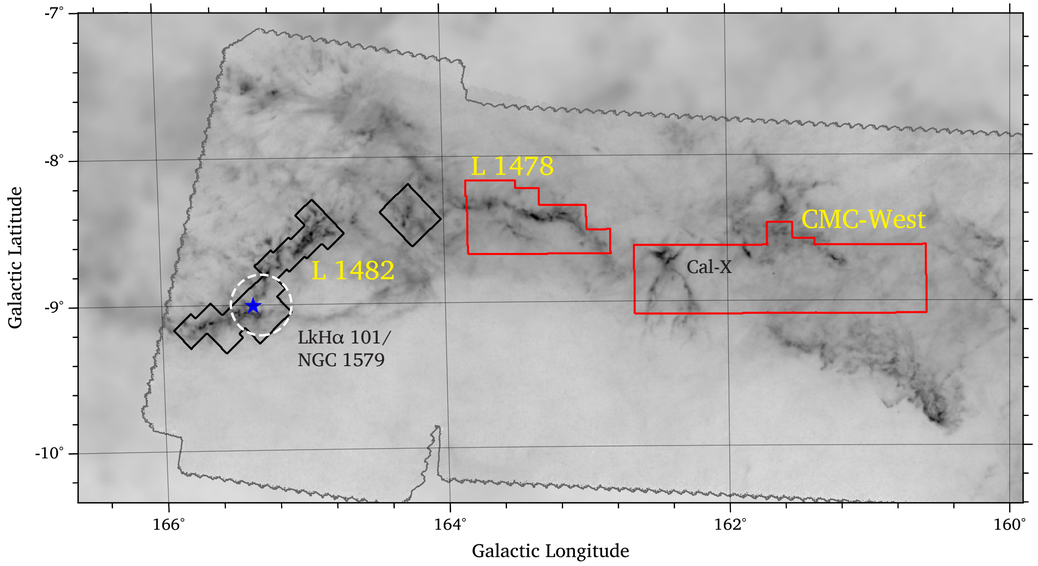

Figure 1. CO survey outlines over *Herschel* +*Planck* dust maps. The CO survey boundary is outlined in black and red, with the black outlined covering L1482, the southeastern extent of the cloud, being initially presented in K15 and the red outlines indicating the new data presented in this paper (L1478, and CMC-West). ^{12}CO and ^{13}CO were observed in all 3 regions, while C^{18}O was not observed in CMC-West. The jagged black boarder marks the extent of the *Herschel* dust data (Lada et al. 2017), with *Planck* data used to fill in outside that. The *Herschel* data continues further west about 1 deg. than shown on the map. The CO survey boarder was chosen to cover the majority of the A_V >3 mag dust. Two subregions of interest are shown. The dashed white circle shows the extent of the H II region (NGC 1579) associated with the star (shown in blue) LkHα 101. In CMC-West we show the Cal-X feature described in Imara et al. (2017).

Table 1. Global ^{12}CO X-factor

Method	X[^{12}CO (2−1)]	K15.
$\langle N[H_2]/W[^{12}CO]\rangle$	5.05 ± 1.80	4.4
$\langle N[H_2]\rangle/\langle W[^{12}CO]\rangle$	4.18 ± 1.83	3.6
Linear fit through origin	2.98 ± 1.74	
Average	**4.1±0.8**	

NOTE—Measurements of the global ^{12}CO (2-1) X-factor for the whole cloud in units of 10^{20} cm^{-2} (K km/s)$^{-1}$. The measurement methods are discussed in §4.2. The K15 are scaled by 1.4 to convert them from the original X_{CO} (1-0) to X_{CO} (2-1).

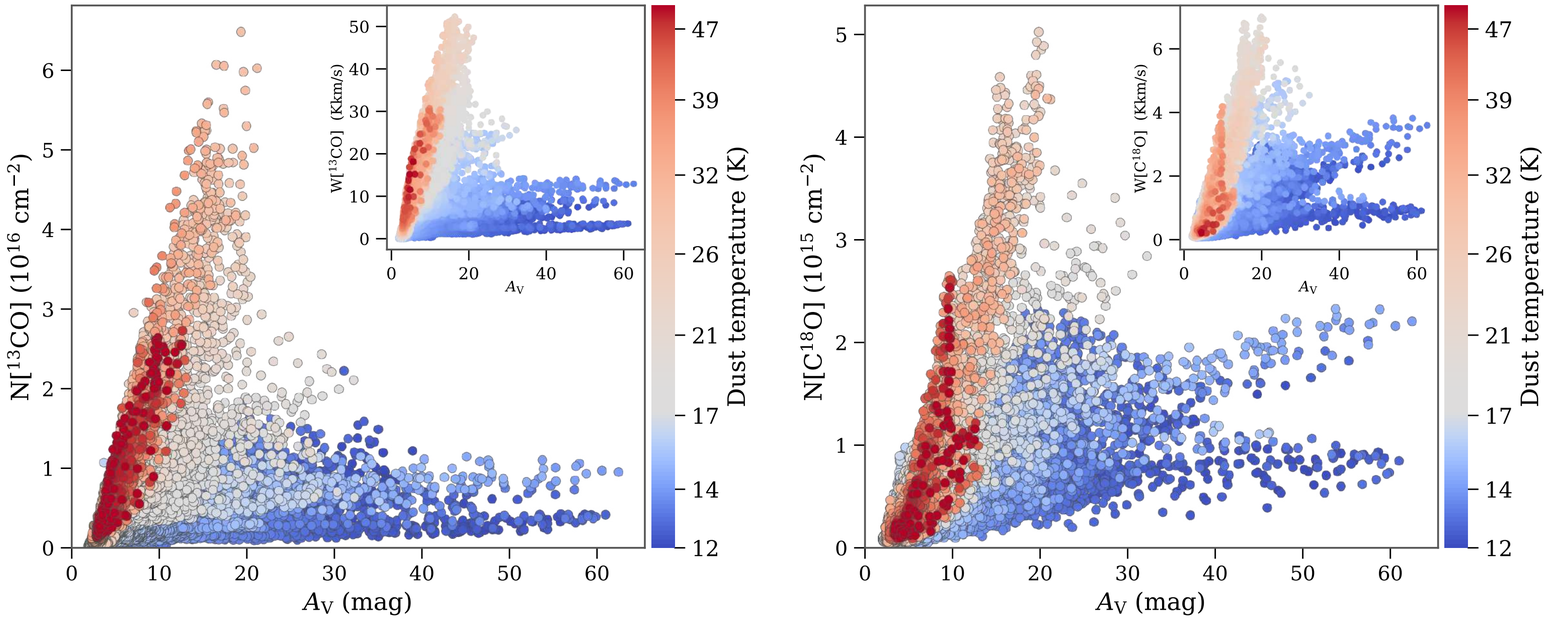

Figure 6. Plot of the (**Left**) ^{13}CO and (**Right**) C^{18}O column density vs visual extinction colored by $T_{\rm dust}$. The colorbar shows colder pixels as blue, transitioning through gray, and becoming redder as the temperature increases. Data is plotted so that higher temperature points are plotted over cooler points to to emphasize the temperature dependent structure in the plot. The inset shows $W_{\rm CO}$ vs $A_{\rm V}$ for the line with the same coloring scheme.

温かい領域 Tdust>25Kで13COとC18Oのアバンダンスを測った結果

$$[^{13}\mathrm{CO}] = (1.31 \pm .89) \times 10^{-6}$$

$$[\mathrm{C}^{18}\mathrm{O}] = (1.27 \pm .59) \times 10^{-7}$$

これはそれぞれstandard atomic abundances ratioですべてのcarbonがCOになっていると仮定したときの値とconsistentらしい[13CO]MW = 1.45×10^−6, [C O]MW = 1.80 × 10^-7

13COとC18Oで同様の図を書いて比較。
cold brancheでは、見積もった光学的厚さは、13COが　1.5, C18O は光学的に薄い(τ 18 < 0.75)
cold branchが３つくらいに分かれているのは場所後がい。L1482とL1478

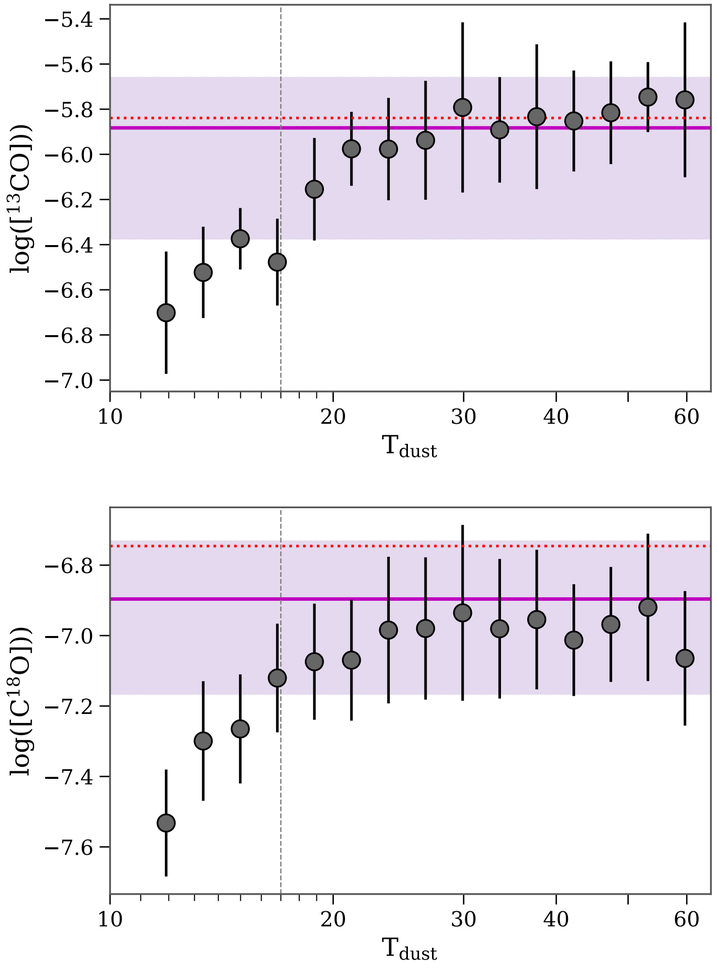

Figure 7. Binned $\log_{10}$ median abundance for (**Top**) ^{13}CO and (**Bottom**) C^{18}O versus dust temperature. The abundance is binned by $T_{\rm dust}$ in logarithmic bins from 10 K - 63 K in 0.05 dex steps. The error-bar is the median absolute deviation scaled to the standard deviation. The purple line with the purple shaded region marks the abundance measured in the hot dust and the corresponding 1σ error. The red dashed line is the cosmic abundance

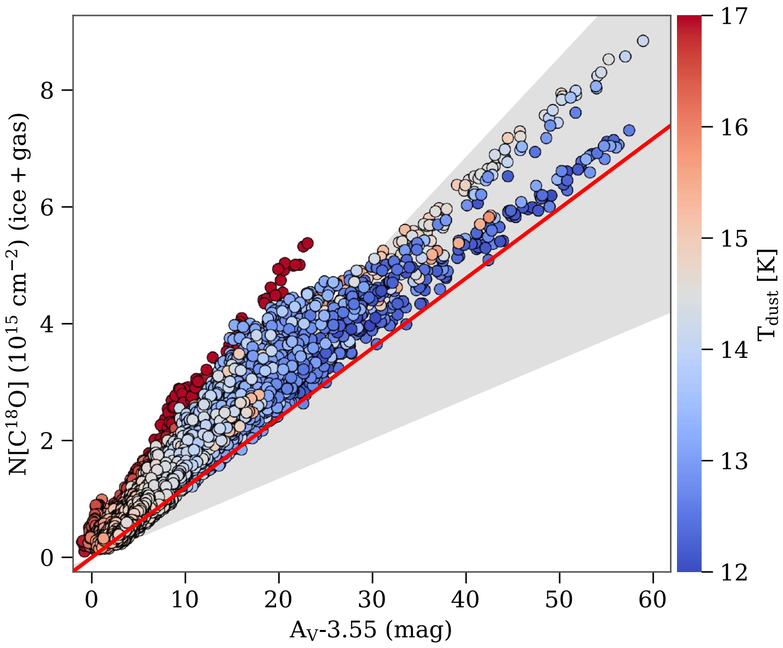

Figure 10. Plot of the total (gas + ice) C^{18}O column density plotted against ($A_{\rm V}-3.55$) mag. The points are colored by $T_{\rm dust}$- note that the scale is different than in Figs. 4 and 6. The red line shows the N[C^{18}O] predicted using the abundance, [C^{18}O] = 1.27×10^{-7} ignoring the material below the 3.55 mag threshold, N[C^{18}O] $\propto$ [C^{18}O]($A_{\rm V}-3.55$). The gray shaded region shows the 1σ uncertainty in the C^{18}O abundance. The total column derived from adding in the contribution from ice is consistent with the total column density derived from the abundance measured in the hot dust.

冷たい領域については、CO氷とCO2氷の量を見積もってたしてやれば、全COの量をだいたいリカバーできる。ここで、COとCO2iceの見積もりはAvから経験的に見積もられている先行研究を使っている。

18. Star Formation Efficiency and Dispersal of Giant Molecular Clouds with UV Radiation Feedback: Dependence on Gravitational Boundedness and Magnetic Fields, Jeong-Gyu Kim, Eve C. Ostriker,1 and Nina Filippova

Molecular clouds are supported by turbulence and magnetic fields, but quantifying their influence on cloud lifecycle and star formation efficiency (SFE) remains an open question. We perform radiation magnetohydrodynamic simulations of star-forming giant molecular clouds (GMCs) with UV radiation feedback, in which the propagation of UV radiation via ray-tracing is coupled to hydrogen photo- chemistry. We consider 10 GMC models that vary in either initial virial parameter ($1 \le \alpha_{\rm vir,0} \le 5$) or dimensionless mass-to-magnetic flux ratio ($0.5 \le \mu_{\Phi,0} \le 8$ and ∞); the initial mass $10^5 M_\odot$ and radius 20pc are fixed. Each model is run with five different initial turbulence realizations. In most models, the duration of star formation and the timescale for molecular gas removal (primarily by pho- toevaporation) are 4-8Myr. Both the final SFE (ε_*) and time-averaged SFE per freefall time ($\varepsilon_{\rm ff}$) are reduced by strong turbulence and magnetic fields. The median ε_* ranges between 2.1% and 9.5%. The median $\varepsilon_{\rm ff}$ ranges between 1.0% and 8.0% and anticorrelates with $\alpha_{\rm vir,0}$, in qualitative agreement with previous analytic theory and simulations. However, the time-dependent $\alpha_{\rm vir}(t)$ and $\varepsilon_{\rm ff,obs}(t)$ based on instantaneous gas properties and cluster luminosity are positively correlated due to rapid evolution, making observational validation of star formation theory difficult. Our median $\varepsilon_{\rm ff,obs}(t) \approx 2\%$ is simi- lar to observed values. We show that the traditional virial parameter estimates the true gravitational boundedness within a factor of 2 on average, but neglect of magnetic support and velocity anisotropy can sometimes produce large departures. Magnetically subcritical clouds are unlikely to represent sites of massive star formation given their unrealistic columnar outflows, prolonged lifetime, and low escape fraction of radiation.

輻射磁気流体シミュレーションをやった。
UVはHydrogen photochemistryとカップルして解いた。
10 GMCモデル。ビリアル比を1-5、mass-to-flux ratioを0.5-8, 無限大、でふった。
初期質量は10^5太陽質量、半径20pcは固定した
どれもだいたい4-8Myrで星形成が終わってガスが飛んでった。

median (時間平均した自由落下時間で割った星形成率) $\varepsilon_{\rm ff}$は、ビリアル比と反相関。

subcriticalクラウドは大質量星形成のサイトとしては不適切そう。

数値計算について

- ベースはAthenaを利用。磁気流体パートは普通。ChemistryはH2, H0, H+を非平衡ちゃんと扱って、C, C+, CO, Oは平衡状態を仮定
- たぶんこの人達が頑張っているのは輻射パート

In addition to Equations (1)–(6), we solve radiative transfer equations in the form

$$\hat{\boldsymbol{n}} \cdot \nabla I = -\kappa I \qquad (7)$$

where I is the intensity, κ is crossection per unit volume in a given radiation component, and $\hat{\mathbf{n}}$ is the direction of ray propagation. The scattering and emission by dust grains are ignored. The radiation field is decomposed into diffuse background and starlight: $I = I^{\rm bg} + I^{*}$. We use the six-ray approximation to solve for the diffuse background, meaning that only $\hat{\boldsymbol{n}}$ aligned with the

- 輻射を２つに分け、diffuse backgroundとstar-light radiationを別々にちゃんと解いた。

計算セットアップのパラメータのフリ方

- 輻射磁気流体シミュレーションをやった。乱流・磁場ありGMC、star clusterからのUV feedbackあり
初期：M0 = 10^5Msun, radius R0 = 20pc, and freefall time tff ,0 = 4.68 Myr.

Table 1. Model parameters

Model	$\alpha_{\rm vir,0}$	$\mu_{\Phi,0}$	$\sigma_{\rm 1d,0}$ [km s^{-1}]	$B_{\rm z,0}$ [μG]	$\mathcal{M}_0$	$\mathcal{M}_{A,0}$
(1)	(2)	(3)	(4)	(5)	(6)	(7)
α-series						
A1B2	1.0	2.0	2.1	13.5	13.6	1.3
A2B2	2.0	2.0	2.9	13.5	19.2	1.9
A3B2	3.0	2.0	3.6	13.5	23.5	2.3
A4B2	4.0	2.0	4.1	13.5	27.2	2.7
A5B2	5.0	2.0	4.6	13.5	30.4	3.0
β-series						
A2B05	2.0	0.5	2.9	54.0	19.2	0.5
A2B1	2.0	1.0	2.9	27.0	19.2	0.9
A2B2	2.0	2.0	2.9	13.5	19.2	1.9
A2B4	2.0	4.0	2.9	6.7	19.2	3.8
A2B8	2.0	8.0	2.9	3.4	19.2	7.6
A2Binf	2.0	∞	2.9	0.0	19.2	∞

運動エネルギー高い

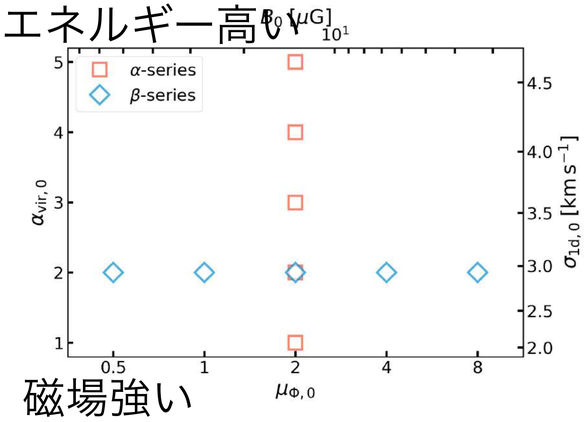

磁場強い

- 簡単な結果
  - すべてのモデルにおいて、UVfeedbackは良く効いて、SFEを下げた。磁場や乱流が強いと更に下がる。
  SFE = 2.1-9.5% (α), 2.4-8.4% (β)
-

- ビリアル比ふったやつ

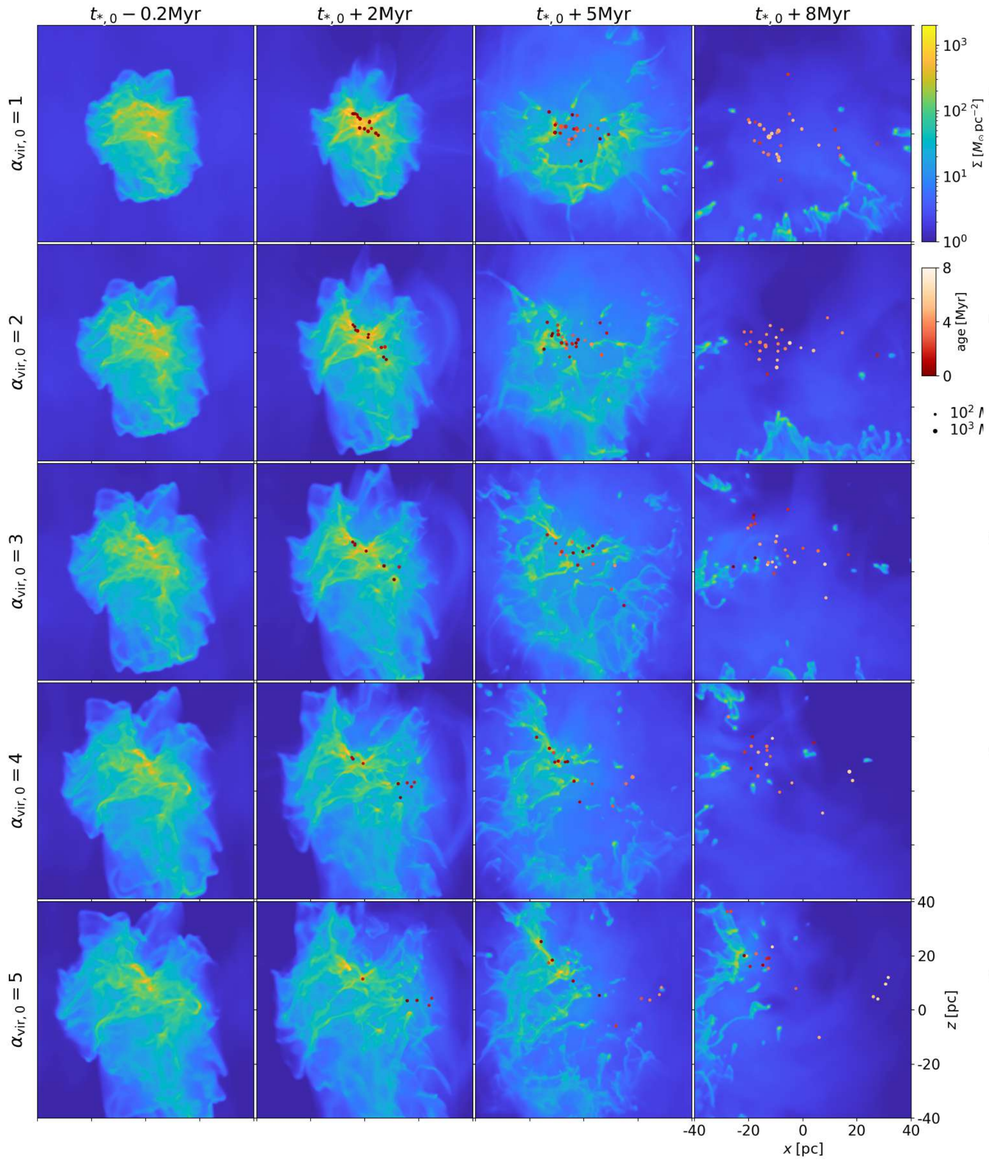

Figure 17. Snapshots of gas surface density projected along the y-axis from the α-series models with `seed` = 4 From top to bottom, the initial virial parameter $\alpha_{\rm vir,0}$ increases from 1 to 5. The projected positions of star particles are indicated by circles. The size and color of circles indicate mass and age, respectively.

- 磁場強度ふったやつ

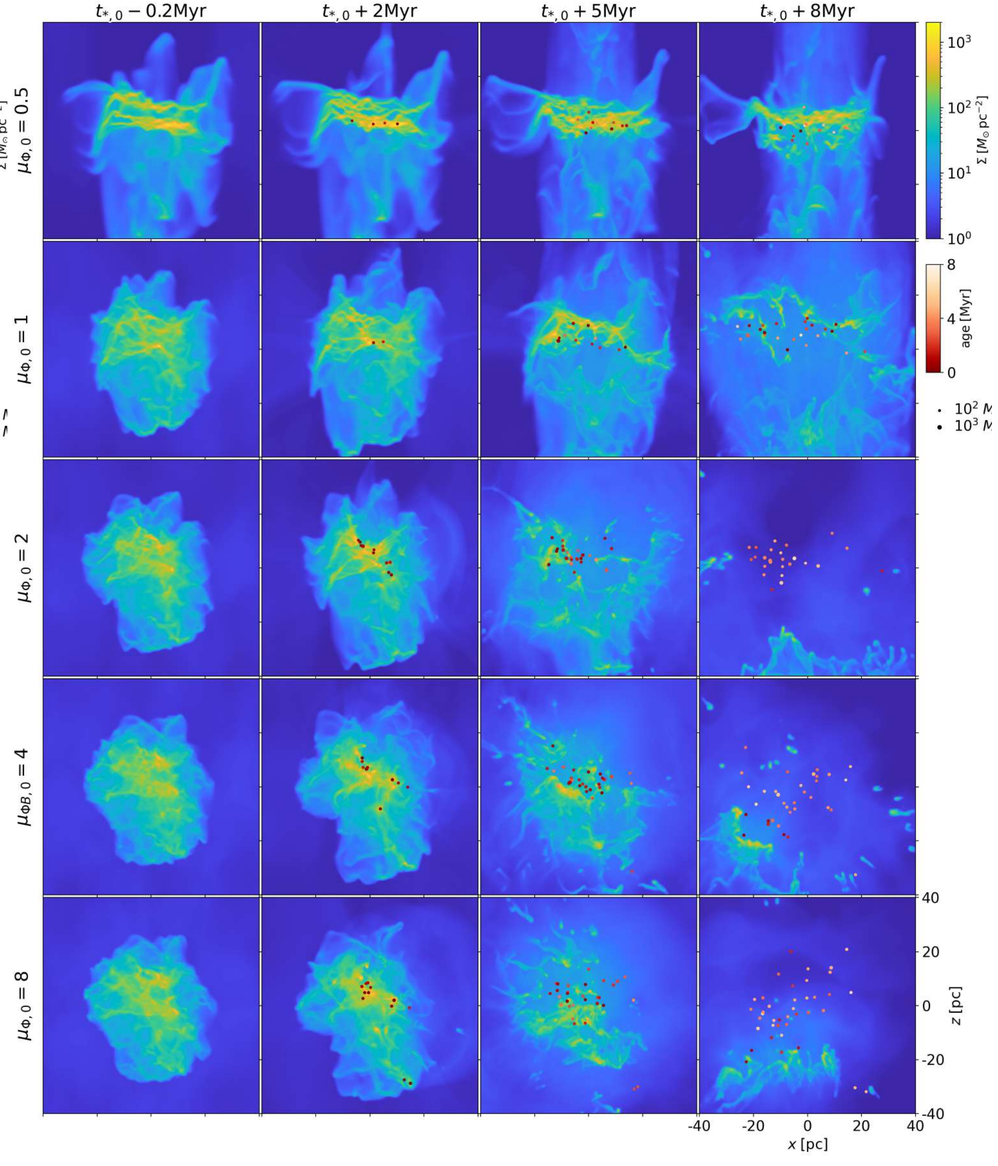

Figure 18. Same as Figure 17 but for the β-series modes with `seed` = 4, which have identical initial turbulent velocity field l varying initial magnetic field strength, decreasing from top to bottom. The corresponding initial mass-to-magnetic flux ra $\mu_{\Phi,0}$ varies from 0.5 to 8.

- 全体の進化について
1. フィラメントができる。 2.sink particleができて、フィラメント内にHII 領域ができる。 3. HII領域が壊れたり合体したりして、光蒸発を促したり、冷たい中性ガスを放出して、星形成を終わらせる。

- 乱流が強いと(αvir>2)クラウドが広がり、OUTFLOWで中性ガスを失う(Fig.17)
- 強い磁場だと(μ<1)フィラメントは初期磁場の方向に垂直になる。動きは非等方になる(Fig.18)

- ビリアル比の時間進化
  - 直接計算したビリアル比と、これまでよく使われていたビリアル比の見積もり$\alpha_{\rm vir}\,^5R\sigma_{\rm 1d}^2/(GM_{\rm neu})\,^1$を比較した。
  - ビリアル比は、乱流が下がるため一旦下がって、それから上がる（feedback）。
  - 初期条件ふったが、最初の星形成の頃に0.5–1.7に落ち着く。磁場が強いと別。
  - 磁場があると、基本的に速度分散から計算した$\alpha_{\rm vir}$を使うと、特に磁場が強いときにビリアル比を過大評価してしまう。

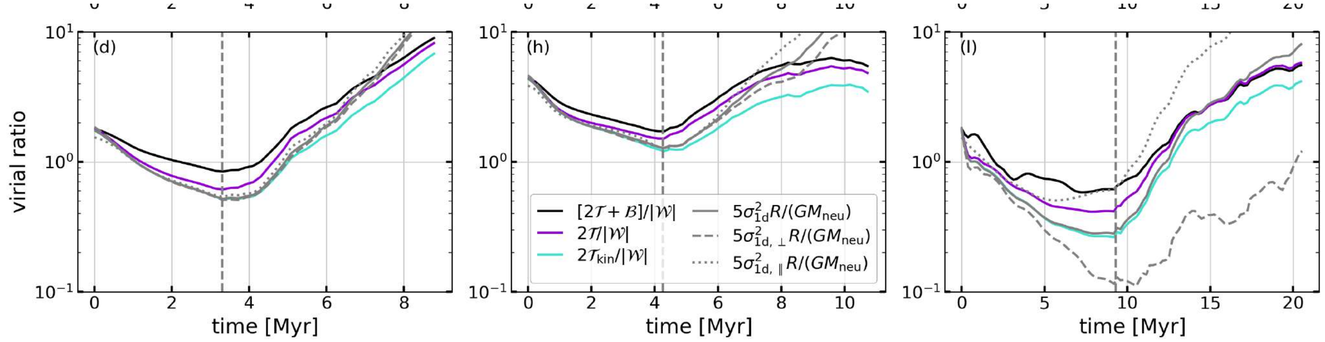

Figure 5. Time evolution of cloud size, velocity dispersion, energy, and virial ratios for three different models `A2B2S4`, `A5B2S4`, and `A2B05S4` until $t_{*,90\%}$, when 90% of the final stellar mass has been formed. The grey dashed vertical lines indicate the time of first star formation. (Top row) The effective radius of neutral cloud $R = 2^{1/3}R_{50\%}$, where $R_{50\%}$ is the half-mass radius. (Second row) Velocity dispersion measured perpendicular ($\sigma_{\rm 1d,\perp}$) and parallel ($\sigma_{\rm 1d,\parallel}$) to the background magnetic field, and averaged over all directions ($\sigma_{\rm 1d}$). (Third row) Gravitational ($|\mathcal{W}|$, blue), kinetic ($\mathcal{T}_{\rm kin}$, red), thermal ($\mathcal{T}_{\rm thm}$, green), and magnetic ($\mathcal{B}$, yellow) energies (see Equations (21)–(24)). A simple estimate of gravitational energy is also shown (blue dashed). (Fourth row) The kinetic virial parameter $\alpha_{\rm vir} = 5\sigma_{\rm 1d}^2R/(GM_{\rm neu})$ for different viewing angles (gray lines) and various energy ratios.

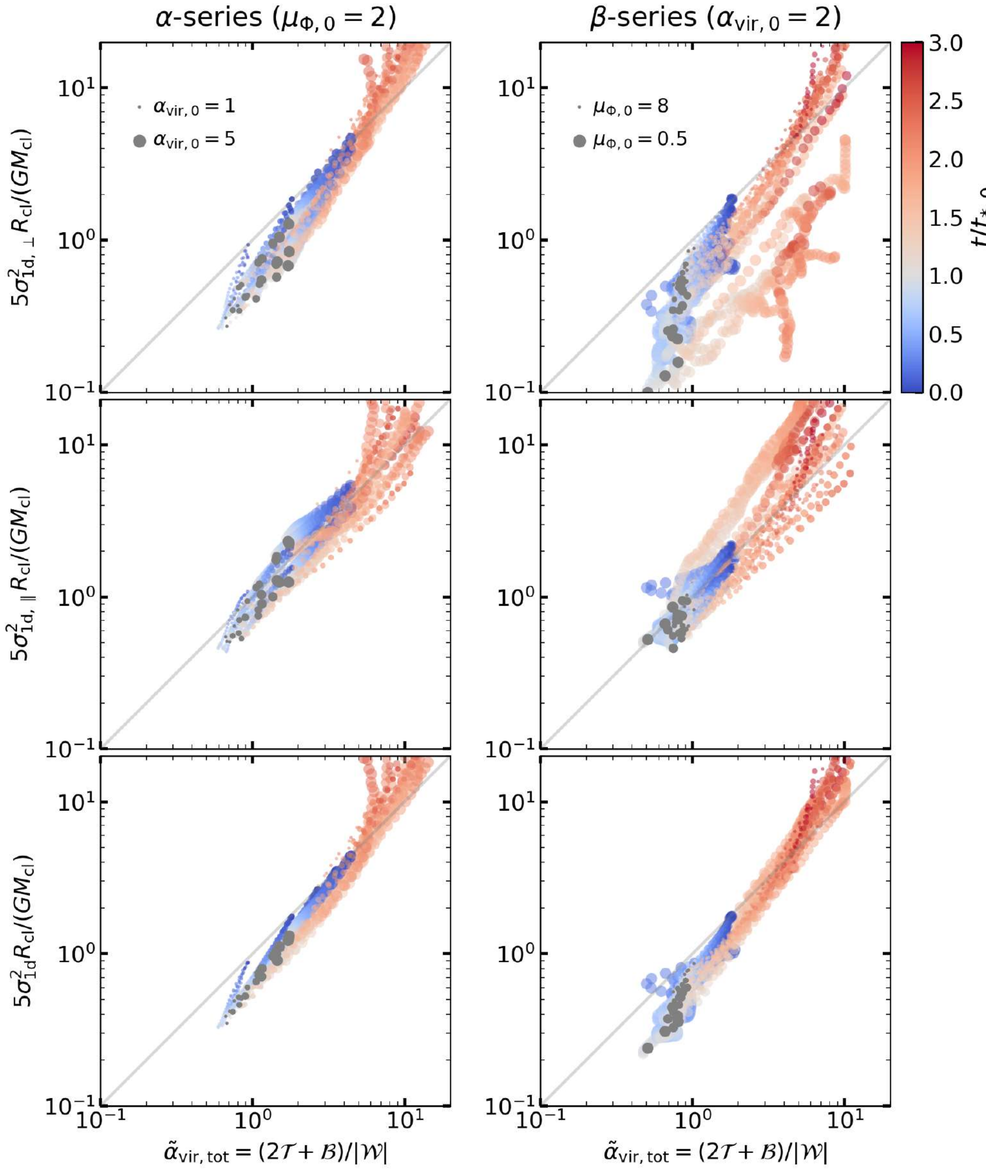

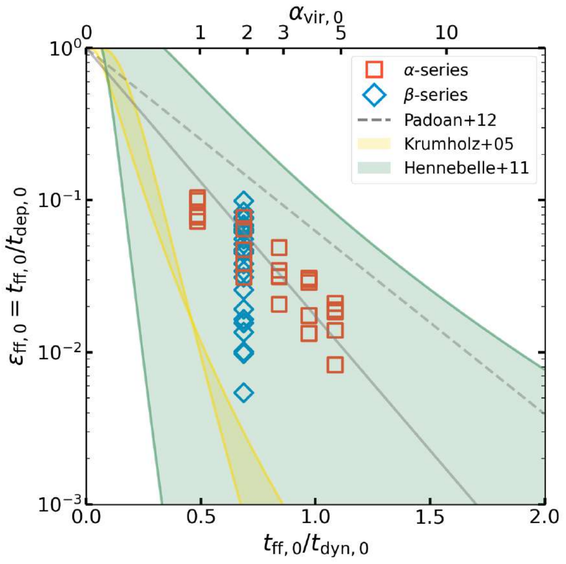

Figure 14. Time-averaged SFE per free fall time defined as $\langle\varepsilon_{\rm ff}\rangle\varepsilon_{\rm ff,0} = t_{\rm ff,0}\langle\dot{M}_*\rangle/M_0 = t_{\rm ff,0}/t_{\rm dep,0}$ as a function of the ratio between the initial freefall and dynamical times in the α-series (red squares) and the β-series (blue diamonds) models. The empirical law $\exp(-1.6\sqrt{3}t_{\rm ff,0}/t_{\rm dyn,0})$ found by Padoan et al. (2012) is shown as a gray dashed line. The gray solid shows the fit to the α-series simulations $\exp(-4.06t_{\rm ff,0}/t_{\rm dyn,0})$. The yellow (green) shaded region is the prediction by the analytic model of Krumholz & McKee (2005) (Hennebelle & Chabrier (2011)) for the Mach number range $13.6 < \mathcal{M} < 30.4$ with $b = 0.5$ and $\beta = 0.02$ (see text for more details).

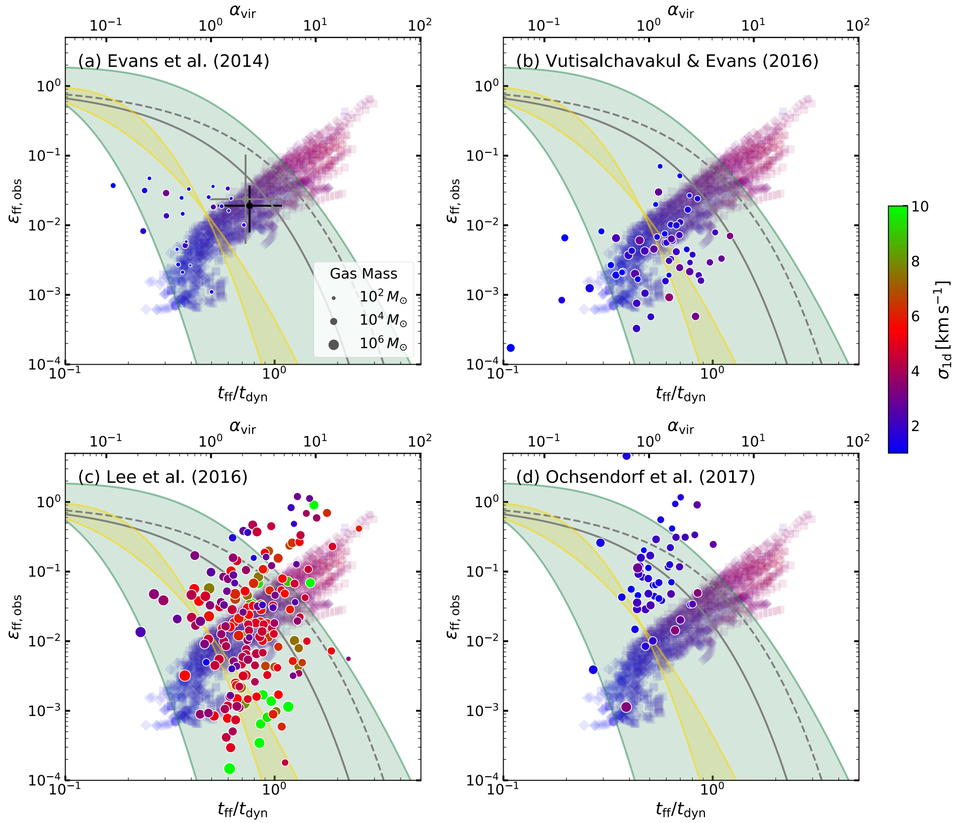

Figure 15. Relation between instantaneous $t_{\rm ff}/t_{\rm dyn} = (\pi^2/40)^{1/2}\alpha_{\rm vir}^{1/2}$ *vs.* $\varepsilon_{\rm ff,obs}$ in simulations (squares and diamonds; α- and β-series models) and observations (circles). For simulations, we use the instantaneous mass, size, and velocity dispersion of the gas cloud and cluster's bolometric UV luminosity. We show snapshots in the time interval $t_{*,0} < t < t_{*,90\%}$. The circles in different panels show data from different observational studies: (a) low-mass, nearby clouds compiled by Evans et al. (2014); (b) molecular clouds in the Galactic Plane with massive star formation rate $M_* > 5\,M_\odot\,{\rm Myr}^{-1}$ (Vutisalchavakul et al. 2016). (c) GMCs with associated star-forming complexes in the Milky Way (Lee et al. 2016). (d) GMCs with associated star-forming complexes in the Large Magellanic Cloud (Ochsendorf et al. 2017). All data points are colored by one-dimensional velocity dispersion $\sigma_{\rm 1d}$ and their sizes denote gas mass. The solid and dashed gray lines, and the yellow and green shaded areas, are based on the same functional forms as in Figure 14, but for instantaneous measurements. In panel (a), the grey bars indicate the ranges of $\varepsilon_{\rm ff,0}$ and $t_{\rm ff,0}/t_{\rm dyn,0}$ plotted in Figure 14, while the black bars indicate the ranges of median values of $\varepsilon_{\rm ff,obs}$ and $t_{\rm ff}/t_{\rm dyn}$ for snapshots between $t_{*,0}$ and $t_{*,90\%}$.

- 星形成率のfreefall time依存性
  - 乱流弱いと高い、磁場弱いと高い
- それを観測と比較すると垂直に交わってる。それを擬似観測で再現できた
  - 輻射でクラウドが大きくなる・質量を失うので、R/Mneuが増える。速度分散も増える。
  - a result, evolution causes $\varepsilon_{\rm ff,obs} \propto M_*(R/M_{\rm neu})^{3/2}$ and $t_{\rm ff}/t_{\rm dyn} \propto \sigma_{\rm 1d}(R/M_{\rm neu})^{1/2}$ to increase in tandem. The

21. Characterization of very wide companion candidates to young stars with planets and disks,
F. Z. Majidi, et al.

Discovering wide companions of stellar systems allows us to constrain the dynamical environment and age of the latter. We studied four probable wide companions of four different stellar systems. The candidates were selected mainly based on their similar kine- matic properties to the central star using Gaia DR2. The central stars are V4046 Sgr, HIP 74865, HIP 65426, and HIP 73145, and their probable wide companions are 2MASS J18152222-3249329, 2MASS J15174874-3028484, 2MASS J13242119-5129503, and 2MASS J14571503-3543505 respectively. V4046 Sgr is a member of β-Pictoris Moving Group while the rest of the stellar systems are acknowledged as members of the Scorpius-Centaurus association. The selected stellar systems are particularly interesting because all of them are already known to possess a low-mass companion and/or a spatially resolved disk. Identifying wider companions of these stars can improve their eligibility as benchmarks for understanding the formation channels of various triple systems, and can help us to determine the orbits of their possibly undiscovered inner, wider companions in case of higher multiplicity. By analyzing the X-Shooter spectra of the wide companion candidates of these stars, we obtained their stellar parameters and determined their ages. We find that 2MASS J15174874-3028484 (0.11 M⊙, 7.4±0.5 Myr), an already recognized pre-main sequence (PMS) member of Scorpius- Centaurus association, is a highly probable wide companion of HIP 74865. 2MASS J13242119-5129503 (0.04 M⊙, 16±2.2 Myr) is ruled out as a plausible wide companion of HIP 65426, but confirmed to be a new sub-stellar member of the Scorpius-Centaurus as- sociation. 2MASS J14571503-3543505 (0.02 M⊙, 17.75±4.15 Myr) is a probable sub-stellar member of the same association, but we cannot confirm whether or not it is gravitationally bound to HIP 73145. 2MASS J18152222-3249329 (0.3 M⊙, older than 150 Myr) is determined to be a mildly active main sequence (MS) star, much older than members of β-Pictoris Moving Group, and unbound to V4046 Sgr despite their similar kinematic features. PMS wide companions such as 2MASS J15174874-3028484 might have formed through cascade fragmentation of their natal molecular core, hinting at high multiplicity in shorter separations which can be confirmed with future observations.

Gaia DR2 のデータを使って、wide companion の候補を4つ持ってきた (V4046 Sgr, HIP 74865, HIP 65426, and HIP 73145,)。

これらの天体はすでに伴星か円盤があることがわかっている。この研究は、そのさらに外側の星を探す。

X-Shooter を使って年齢を推定。4つについてそれぞれ議論した。

Table 1: Physical parameters of the central stars.

Name	Distance [a] (pc)	Association	SpT	$T_{\rm eff}$ (K)	A_v (mag)	Wide companion	Separation (″)	Separation (au)
V4046Sgr	72.4	β-Pictoris MG	K5/K7	4370/4100	0 [b]	2MASS J1815-3249	901	65232
HIP 74865	123.53	Sco-Cen (UCL)	F3V	6720	0	2MASS J1517-3028	90	11118
HIP 65426	109.21	Sco-Cen (LCC)	A2V	8840	0	2MASS J1324-5129	142	15508
HIP 73145	133.65	Sco-Cen (UCL)	A2IV	8840	0	2MASS J1457-3543	280	37422
GQ Lup	151.82	Sco-Cen (Lupus I)	K7V	4070	0.7 [c]	2MASS J1549-3539	16	2429

[a] Distances are calculated based on the parallaxes of the objects reported in *Gaia* DR2 catalog.
[b] (Stempels & Gahm 2004)
[c] (Alcalá et al. 2017)

イントロ

・Gaiaの感度だと、褐色矮星の伴星 <20Myr, <150pcくらいのものは見つけられる。

・SPHERE-GTOターゲットの中で、Gaia DR2で伴星っぽいものを探す→数十ターゲット。

・分光観測して、若い天体に絞る。→表の通り

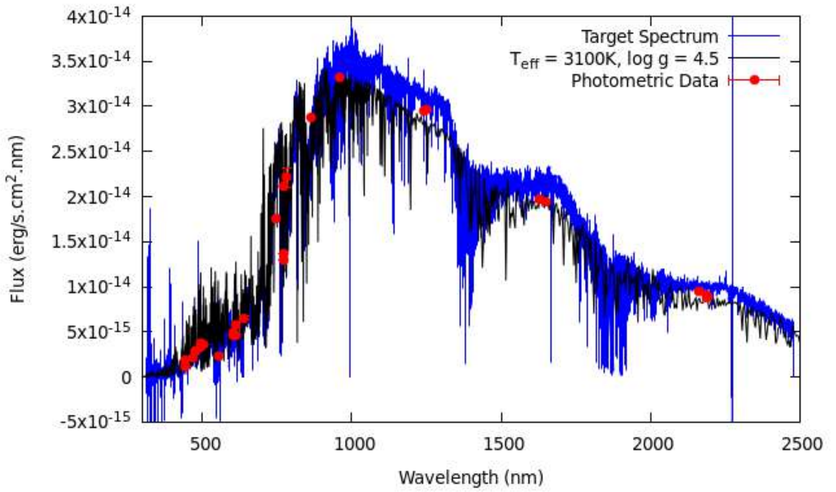

Fig. 2: Spectrum of 2MASS J1517-3028 (blue) together with the available photometric data (red dots) in the literature and the fitted BT-Settl model (black).

Table 3: Physical stellar parameters of candidates. Except for 2MASS J1815-3249, mass, age, and log g are selected from the closest matches offered by Baraffe et al. (2015) models. The same quantities are extracted from MIST isochrones for 2MASS J1815-3249.

Name	SpT	$T_{\rm eff}$ (K)	A_v (mag)	RV (km/s)	$L_\star$ ($L_\odot$)	$R_\star$ ($R_\odot$)	$M_\star$ ($M_\odot$)	Age (Myr)	log g
2MASS J1815-3249	M3±0.5	3410	0	−17.7±2.4	0.03	0.5	0.3	> 150	4.95
2MASS J1517-3028	M4.5±0.5	3100	0	1.2±6.9	0.018	0.47	0.11	7.9	4.13
2MASS J1324-5129	M6.5±0.5	2710	0	15.3±5.8	0.0024	0.22	0.04	18.2	4.35
2MASS J1457-3543	M8±0.5	2500	0	4.0±8.9	0.002	0.24	0.02	14.09	4.00
2MASS J1549-3539	M4±0.5	3190	1.0±0.5	−1.3±4.0	0.07 [a]	0.21	0.15	2	3.78

[a] This object is sub-luminous. The value reported here is the object's corrected luminosity obtained by Alcalá et al. (2020).

Table 4: ROTFIT results acquired for the targets. The estimated ages are concluded from Baraffe et al. (2015) models.

Name	$T_{\rm eff}$ (K)	log g	RV (km/s)	$v \sin i$ (km/s)	Age (Myr)
2MASS J1815-3249	3562±30	4.68±0.14	−20.1±2.0	< 8.0	> 150
2MASS J1517-3028	3077±22	4.49±0.21	1.4±2.4	26±6	7.4±0.5
2MASS J1324-5129	2646±50	4.0±0.1	17.9±3.0	< 8.0	16±2.2
2MASS J1457-3543	2635±80	4.30±0.17	8.0±7.8	62.0±10.0	17.75±4.15
2MASS J1549-3539	3230±101	3.74±0.23	−2.0±2.8	13.0±6.0	2.75±0.75

Table 8: The wide-companion membership status checklist for our targets.

Name	Consistent kinematic properties with the stellar system (yes/no)	Age (MS/PMS)	Active (yes/no)	Contains Li I (yes/no)	conclusion
2MASS J1815-3249	no	MS	no	no	field object
2MASS J1517-3028	yes	PMS	yes	yes	UCL member + HIP 74865 probable wide companion
2MASS J1324-5129	no	PMS	yes	yes	LCC new member
2MASS J1457-3543	no	PMS	yes	ambiguous	ambiguous
2MASS J1549-3539	yes	PMS	yes	yes	Lupus I new member + GQ Lup probable wide companion

結論

V4046 Sgr - 候補生 2MASS J1815-3249は関係ない単独星だった。残念。

HIP 74865 and GQ Lupi:

重たい星のすぐ近くを褐色矮星が周り、遠くに遠隔伴星がいるシステム。

HIP 65426 - 2MASS J1324-5129 とは関係なさそう。

HIP 73145: 2MASS J1457- 3543. とは関係なさそう

面白そうな天体の簡易まとめ

HIP 74865について：F3V型, Sco-Cen association, 16auのところに褐色矮星がいる、SPHEREで取られている、質量0.17Msun、2MASS J1517-3028 のseparationは11118 au

GQ Lupiについて：K7V型、Sco-Cen (Lupus I) , 若い2Myr、GQLup Bが20-40 M jup、円盤ある、2MASS J1549-3539 のseparationは2429au

A new prolonged decrease event in the brightness of the young stellar object V2492 Cygni

Sunay Ibryamov, Evgeni Semkov

Results from the BV(RI)c photometric observations of the young stellar object V2492 Cyg collected in the period from April 2018 to September 2020 are presented. These observations are a part of our monitoring of the star that began in 2010 and continuing to date. V2492 Cyg is located in the Pelican Nebula, and its variability was explained by both accretion and extinction events. The new photometric data show that the star continues to exhibit rapid irregular variability in all bands. In the period from March 2019 to May 2020, we registered a prolonged decrease event in the light curve of V2492 Cyg.

- V2492 Cygという星の2018-2020年のモニタリング報告。
- プロジェクト自体は2010年から。
- 継続的に変動を見せ続けている。
- March 2019 からMay 2020にかけて、の減光イベントを同定

19. The CARMA-NRO Orion Survey: Filament Formation via Collision-Induced Magnetic Reconnection – The Stick in Orion A, Shuo Kong, et al.

A unique filament is identified in the Herschel maps of the Orion A giant molecular cloud. The filament, which, we name the Stick, is ruler-straight and at an early evolutionary stage. Transverse position-velocity diagrams show two velocity components closing in on the Stick. The filament shows consecutive rings/forks in C18O(1-0) channel maps, which is reminiscent of structures generated by magnetic reconnection. We pro- pose that the Stick formed via collision-induced magnetic reconnection (CMR). We use the magnetohydrodynamics (MHD) code Athena++ to simulate the collision between two diffuse molecular clumps, each carrying an anti-parallel magnetic field. The clump collision produces a narrow, straight, dense filament with a factor of >200 increase in density. The production of the dense gas is seven times faster than free-fall collapse. The dense filament shows ring/fork-like structures in radiative transfer maps. Cores in the filament are confined by surface magnetic pressure. CMR can be an important dense-gas-producing mechanism in the Galaxy and beyond.

ハーシェルで見つかったOrionA分子雲のフィラメントについて。Stickと名付けた。

PV図解析でみると、2つのコンポーネントがみえる。

Stickは、衝突励起の磁気リコネクションで形成されたと提案する
Athna++で2つの分子クランプの衝突を計算、200倍くらい密度の高いフィラメントを再現。自由落下よりも7倍早くフィラメントを作れる

ring/fork-like構造も作れる。

The Cloud Factory II: Gravoturbulent Kinematics of Resolved Molecular Clouds in a Galactic Potential

Andres F. Izquierdo, Rowan J. Smith, Simon C. O. Glover, Ralf S. Klessen, Robin G. Tress, Mattia C. Sormani, Paul C. Clark, Ana Duarte-Cabral, Catherine Zucker

We present a statistical analysis of the gravoturbulent velocity fluctuations in molecular cloud complexes extracted from our "Cloud Factory" galactic-scale ISM simulation suite. For this purpose, we produce non-LTE ^{12}CO J=1-0 synthetic observations and apply the Principal Component Analysis (PCA) reduction technique on a representative sample of cloud complexes. The velocity fluctuations are self-consistently generated by different physical mechanisms at play in our simulations, which include galactic-scale forces, gas self-gravity, and supernova feedback. The statistical analysis suggests that, even though purely gravitational effects are necessary to reproduce standard observational laws, they are not sufficient in most cases. We show that the extra injection of energy from supernova explosions plays a key role in establishing the global turbulent field and the local dynamics and morphology of molecular clouds. Additionally, we characterise structure function scaling parameters as a result of cloud environmental conditions: some of the complexes are immersed in diffuse (inter-arm) or dense (spiral-arm) environments, and others are influenced by embedded or external supernovae. In quiescent regions, we obtain time-evolving trajectories of scaling parameters driven by gravitational collapse and supersonic turbulent flows. Our findings suggests that a PCA-based statistical study is a robust method to diagnose the physical mechanisms that drive the gravoturbulent properties of molecular clouds. Also, we present a new open source module, the PCAFACTORY, which smartly performs PCA to extract velocity structure functions from simulated or real data of the ISM in a user-friendly way. Software DOI: 10.5281/zenodo.3822718

- Cloud Factory というシミュレーション結果の解析の一つ
- 分子雲におけるgravoturbulent velocity fluctuationの解析を主たる目的とした。
- non_LTE 12COの疑似観測をやってPCA解析。
- 結果：乱流状態と分子雲のダイナミクスと形を再現するには、超新星爆発のようなエネルギー注入が重要であることがわかった。

Evolution of the density PDF in star forming clouds: the role of gravity

Etienne Jaupart, Gilles Chabrier

We derive an analytical theory of the PDF of density fluctuations in supersonic turbulence in the presence of gravity in star-forming clouds. The theory is based on a rigorous derivation of a combination of the Navier- Stokes continuity equations for the fluid motions and the Poisson equation for the gravity. It extends upon previous approaches first by including gravity, second by considering the PDF as a dynamical system, not a stationary one. We derive the transport equations of the density PDF, characterize its evolution and determine the density threshold above which gravity strongly affects and eventually dominates the dynamics of turbulence. We demonstrate the occurence of two power law tails in the PDF, with two characteristic exponents, corresponding to two different stages in the balance between turbulence and gravity. Another important result of this study is to provide a procedure to relate the observed column density PDFs to the corresponding volume density PDFs. This allows to infer, from the observation of column-densities, various physical parameters characterizing molecular clouds, notably the virial parameter. Furthermore, the theory offers the possibility to date the clouds in units of tcoll, the time since a statistically significant fraction of the cloud started to collapse. The theoretical results and diagnostics reproduce very well numerical simulations and observations of star-forming clouds. The theory provides a sound theoretical foundation and quantitative diagnostics to analyze observations or numerical simulations of star-forming regions and to characterize the evolution of the density PDF in various regions of molecular clouds.

- 分子雲における、超音速乱流下での密度関数を解析的に求めた。
- ナビエ・ストークスの連続の式と、重力についてはポアソン方程式を使った。
- PDF の移流方程式をだした。
- 結果、乱流と重力の釣り合いにより、二個のパワーローが出てくる。
- 観測される面密度PDFへのから空間密度PDFへの関係性も示した。